

MONTE CARLO STUDY OF ELECTRON AND POSITRON COSMIC-RAY PROPAGATION WITH THE CALET SPECTRUM

KATSUAKI ASANO¹, YOICHI ASAOKA¹, YOSUI AKAIKE^{2,3}, NORITA KAWANAKA^{4,5,6}, KAZUNORI KOHRI^{7,8}, HOLGER M. MOTZ⁹, TOSHIO TERASAWA¹

¹Institute for Cosmic Ray Research, The University of Tokyo, 5-1-5 Kashiwanoha, Kashiwa, Chiba 277-8582, Japan

²Waseda Research Institute for Science and Engineering, Waseda University, 17 Kikuicho, Shinjuku, Tokyo 162-0044, Japan

³JEM Utilization Center, Human Spaceflight Technology Directorate, Japan Aerospace Exploration Agency, 2-1-1 Sengen, Tsukuba, Ibaraki 305-8505, Japan

⁴Hakubi Center, Kyoto University, Yoshida Honmachi, Sakyo-ku, Kyoto 606-8501, Japan

⁵Department of Astronomy, Graduate School of Science, Kyoto University, Kitashirakawa Oiwake-cho, Sakyo-ku, Kyoto 606-8502, Japan

⁶Yukawa Institute for Theoretical Physics, Kyoto University, Kitashirakawa Oiwake-cho, Sakyo-ku, Kyoto 606-8502, Japan

⁷Theory Center, IPNS, KEK, and SOKENDAI, 1-1 Oho, Tsukuba, Ibaraki 305-0801, Japan

⁸Kavli IPMU (WPI), UTIAS, The University of Tokyo, Kashiwa, Chiba 277-8583, Japan and

⁹Faculty of Science and Engineering, Global Center for Science and Engineering, Waseda University, 3-4-1 Okubo, Shinjuku, Tokyo 169-8555, Japan

Draft version November 19, 2021

ABSTRACT

Focusing on the electron and positron spectrum measured with CALET, which shows characteristic structures, we calculate flux contributions of cosmic rays escaped from supernova remnants, which were randomly born. We adopt a Monte Carlo method to take into account the stochastic property of births of nearby sources. We find that without a complicated energy dependence of the diffusion coefficient, simple power-law diffusion coefficients can produce spectra similar to the CALET spectrum even with a dispersion in the injection index. The positron component measured with AMS-02 is consistent with a bump-like structure around 300 GeV in the CALET spectrum. One to three nearby supernovae can contribute up to a few tens of percent of the CALET flux at 2–4 TeV, ten or more unknown and distant ($\gtrsim 500$ pc) supernovae account for the remaining several tens of percent of the flux. The CALET spectrum, showing a sharp drop at ~ 1 TeV, allows for a contribution of cosmic rays from an extraordinary event which occurred ~ 400 kyr ago. This type of event releases electrons/positrons with a total energy more than 10 times the average energy for usual supernovae, and its occurrence rate is lower than 1/300 of the usual supernova rate.

Subject headings: astroparticle physics — cosmic rays — supernova remnants

1. INTRODUCTION

Direct measurements of electron and positron cosmic-rays (CRs) have been pioneered by various teams such as BETS (Torii et al. 2001), HEAT (DuVernois et al. 2001), ATIC (Chang et al. 2008), PPB-BETS (Yoshida et al. 2008), and PAMELA (Adriani et al. 2011). Recently, the electron and positron CR study (total CR flux not distinguishing their charge signs) has been greatly advanced with new instruments such as AMS-02 (Aguilar et al. 2014, 2019), *Fermi*-LAT (Abdollahi et al. 2017), CALET (Adriani et al. 2017, 2018; Torii & Akaike 2021), and DAMPE (Ambrosi et al. 2017). While the spectra of electron and positron CRs measured with AMS-02 and CALET are consistent, the spectra obtained with *Fermi*-LAT and DAMPE show slightly harder shape and higher fluxes above 300 GeV. The discrepancy between the spectra reported by the different teams has not been resolved yet.

The CALET and DAMPE collaborations reported the spectra as far as 4.6–4.8 TeV (Ambrosi et al. 2017; Adriani et al. 2018). The DAMPE team claimed the detection of a spectral break at \sim TeV (Ambrosi et al. 2017), and the CALET spectrum also suggests a softening above \sim TeV (Adriani et al. 2018). The recent preliminary results with CALET also confirm

a broken power-law at \sim TeV with higher statistics (Torii & Akaike 2021). The TeV break can be attributed to the radiative cooling effect (Lipari 2019; Mertsch 2018), or to electron-positron pairs coming from a single nearby pulsar wind nebula (PWN) like Monogem (Ding et al. 2021). Kisaka & Kawanaka (2012) and Shi & Liu (2019) proposed models with millisecond pulsars as sources of CR components responsible for the TeV break.

As the cooling timescale for TeV electrons is short, the sources of TeV electron/positron CRs must be nearby. Possible sources are known pulsars like the Vela pulsar (Huang et al. 2018), unknown multiple pulsars (Kawanaka et al. 2011; Cholis et al. 2018), known supernova remnants (SNRs) like Vela (Kobayashi et al. 2004) or Cygnus Loop (Manconi et al. 2019), unknown old SNRs (Fang et al. 2018; Fornieri et al. 2020), and white dwarf pulsars (Kashiyama et al. 2011). The small number of nearby sources implies a large dispersion in the predicted TeV flux as discussed in Kawanaka et al. (2010); Cholis et al. (2018); Fang et al. (2018); Mertsch (2018).

As a conservative approach, the difference between DAMPE and CALET spectra could be treated as systematic errors. In this paper, however, we focus on only the CALET spectrum with its characteristic structures: a spectral bump around 200–300 GeV, and a sharp flux drop at ~ 1 TeV. Since the CALET and

AMS-02 spectra of electron and positron CRs are consistent, it may be reasonable to discuss the CALET electron and positron spectrum together with the positron spectrum measured with AMS-02 (Accardo et al. 2014; Aguilar et al. 2019). The positron component above 100 GeV is apparently a different component from the electron component, which dominates the electron and positron flux. Potential sources of positrons above 100 GeV are pulsars (Cholis et al. 2018; Di Mauro et al. 2021; Orusa et al. 2021) or a single SNR interacting dense medium (Fujita et al. 2009; Kohri et al. 2016). The spectral bump in the CALET spectrum may be attributed to the positron component.

The dominant component of electron and positron CRs are electrons from SNRs. To investigate the effect of the number fluctuation of nearby sources, we adopt a Monte Carlo method in our calculations (see also Mertsch 2018; Evoli et al. 2021; Orusa et al. 2021). We examine whether SNRs, which randomly occur, can reproduce the characteristic structures in the CALET spectrum, or if different origins are required. Compared to the previous study by Evoli et al. (2021), we focus more on the modulation of the CALET spectrum. We also study the influence of the variation in the injection spectra on the total spectrum. The dispersion in the injection index was taken into account for pulsars in Cholis et al. (2018). In our study, the variation of the injection index is introduced for electron CRs from SNRs as well. A very large dispersion in the injection spectral index may contradict the observed spectrum.

In this paper, we adopt the officially published data of the electron and positron spectrum with CALET (Adriani et al. 2018), which is consistent with the preliminary updated result of Torii & Akaike (2021).

2. NUMERICAL METHODS

We calculate the CR flux at the earth by integrating the contributions of individual sources. We use the standard Green's function method to estimate the contribution of a single source (Atoyan et al. 1995). First, we review the calculation method for a single source.

2.1. CR Propagation

The number density spectrum of electrons/positrons $n(\gamma)$ from a single source at the origin $r = 0$ in spherical coordinates is calculated with the diffusion equation,

$$\frac{\partial n}{\partial t} - K \frac{1}{r^2} \frac{\partial}{\partial r} \left(r^2 \frac{\partial n}{\partial r} \right) + \frac{\partial}{\partial \gamma} (\dot{\gamma} n) = Q_{\text{inj}}(\gamma), \quad (1)$$

where Q_{inj} is the injection term, and the diffusion coefficient in the second term is assumed as a power-law function of energy,

$$K(\gamma) = K_0 \left(\frac{\gamma m_e c^2}{\text{GeV}} \right)^q. \quad (2)$$

In the simplest model with isotropic Alfvén turbulence, the index q is related to the power-law index for the power spectrum of the turbulence in the interstellar medium. The standard Kolmogorov turbulence ($q = 1/3$) and Iroshnikov–Kraichnan turbulence ($q = 1/2$) are representative models.

The radiative cooling effect in the third term of equation (1) includes synchrotron (SYN) cooling and inverse

Compton (IC) cooling as

$$\dot{\gamma} m_e c^2 = -b_{\text{IC}}(\gamma) - b_{\text{SYN}}(\gamma). \quad (3)$$

The synchrotron cooling term is written as

$$b_{\text{SYN}}(\gamma) = \frac{4}{3} \sigma_{\text{T}} c \frac{B^2}{8\pi} \gamma^2, \quad (4)$$

where σ_{T} is the cross section of the Thomson scattering. Below we adopt the magnetic field of $B = 3\mu\text{G}$. For the IC cooling term b_{IC} , we take into account the Klein–Nishina effect as explained below.

When an electron with Lorentz factor γ is in a photon field of the spectral density $n_{\text{ph}}(\varepsilon_0)$, the photon production rate of an energy ε_1 via IC is

$$\begin{aligned} \dot{N}(\varepsilon_0, \varepsilon_1) &= \frac{3\sigma_{\text{T}}c}{4\varepsilon_0\gamma^2} n_{\text{ph}}(\varepsilon_0) \\ &\times \left[2q \ln q + (1+2q)(1-q) + \frac{(\Gamma q)^2}{2(1+\Gamma q)}(1-q) \right], \end{aligned} \quad (5)$$

where

$$q \equiv \frac{x_1}{\Gamma(1-x_1)}, \quad x_1 \equiv \frac{\varepsilon_1}{\gamma m_e c^2}, \quad \Gamma \equiv \frac{4\gamma\varepsilon_0}{m_e c^2}, \quad (6)$$

(e.g. Blumenthal & Gould 1970; Delahaye et al. 2010). With this photon production rate, the cooling rate via IC is written as

$$b_{\text{IC}}(\gamma) = \int d\varepsilon_0 \int d\varepsilon_1 (\varepsilon_1 - \varepsilon_0) \dot{N}(\varepsilon_0, \varepsilon_1). \quad (7)$$

This is rewritten with $x_1 = \Gamma q / (1 + \Gamma q)$ and $dx_1 = \Gamma / (1 + \Gamma q)^2 dq$ as

$$\begin{aligned} b_{\text{IC}}(\gamma) &= \int d\varepsilon_0 \int_{1/(4\gamma^2)}^1 dq \frac{\Gamma^2 (\gamma m_e c^2)^2}{(1 + \Gamma q)^2} \\ &\times \left(\frac{q}{1 + \Gamma q} - \frac{1}{4\gamma^2} \right) \dot{N}(\varepsilon_0, \varepsilon_1). \end{aligned} \quad (8)$$

We consider a case in which the photon field is approximated by the diluted Planck distribution,

$$n_{\text{ph}}(\varepsilon_0) = \frac{15U_{\text{ph}}}{(\pi T)^4} \frac{\varepsilon_0^2}{\exp(\varepsilon_0/T) - 1}, \quad (9)$$

where U_{ph} and T are the photon energy density and temperature, respectively. In this case, the Klein–Nishina effect is separately represented by a dimensionless factor f_{KN} as

$$b_{\text{IC}}(\gamma) = \frac{4}{3} \sigma_{\text{T}} c U_{\text{ph}} \gamma^2 f_{\text{KN}}(\gamma, T). \quad (10)$$

Defining dimensionless quantities $y = \varepsilon_0/T$ and $z = 4\gamma T / (m_e c^2)$, we can write $\Gamma = yz$, then the factor f_{KN}

is expressed as a function of z as

$$f_{\text{KN}}(z) = \frac{135}{\pi^4} \int dy \frac{y^3}{\exp(y) - 1} \times \int_{1/(4\gamma^2)}^1 dq \frac{1}{(1 + yzq)^2} \left(\frac{q}{1 + yzq} - \frac{1}{4\gamma^2} \right) \times \left[2q \ln q + (1 + 2q)(1 - q) + \frac{(yzq)^2}{2(1 + yzq)}(1 - q) \right]. \quad (11)$$

While $f_{\text{KN}}(z) \simeq 1$ for $z \ll 1$,

$$f_{\text{KN}}(z) \simeq \frac{45}{4\pi^2 z^2} (\ln z - 1.9805), \quad (12)$$

for $z \gg 1$. For the numerical approximation of the function $f_{\text{KN}}(z)$, we use the fitting formulae in Fang et al. (2021) in our numerical calculation.

Following Delahaye et al. (2010); Evoli et al. (2020), the photon field in the interstellar space is modeled by a sum of 6 diluted Planck distributions: $T = 2.725, 33.07, 313.32, 3249.3, 6150.4, \text{ and } 23209.0$ K with $U_{\text{ph}} = 0.26, 0.25, 0.055, 0.37, 0.23, \text{ and } 0.12$ eV cm $^{-3}$, respectively.

2.2. CR Injection

Let us assume the power-law plus exponential cutoff for the injection spectrum from a CR source at a distance r_i and the CR release time $t = -t_i$ as

$$Q_{\text{inj}}(\gamma) = Q_i \left(\frac{\gamma m_e c^2}{\text{GeV}} \right)^{-\alpha} \exp \left(-\frac{\gamma}{\gamma_{\text{max}}} \right) \delta(\mathbf{r} - \mathbf{r}_i) \delta(t + t_i), \quad (13)$$

which is expressed by three parameters, the normalization Q_i , the spectral index α , and the cutoff Lorentz factor γ_{max} .

Here, we approximate the injection process by prompt injections. Note that the spectral shape in equation (13) is an effective one after the escape process from the source. The spectral shape of escaped CRs largely depends on the escape and the cooling processes, which are observationally and theoretically uncertain. Although the injection is generally time-dependent, we approximate the injection process using equation (13) as a CR spectrum at the escape time $t = -t_i$.

At the earth, multiple sources with different distances r_i and ages t_i contribute to the electron and positron CR spectrum. To integrate these contributions, we carry out Monte Carlo simulations for a distribution of sources in distance and age. The primary sources of electron cosmic-rays are SNRs. The total energy of CR electrons escaping from a SNR,

$$E_{\text{tot}} = \int_{\gamma_m}^{\infty} d\gamma Q_{\text{inj}}(\gamma) \gamma m_e c^2, \quad (14)$$

is fixed to 9.0×10^{47} erg, which is about 0.1 % of the explosion energy of a supernova (SN), and 1 % of the CR proton energy. The total CR energy is defined by integrating above 1 GeV, so that the lower bound in the above integral is $\gamma_m \simeq 1960$.

We also consider pulsars as sources of electron–positron CRs. Several models of a significant contribution from

Geminga pulsar have been proposed as explanation for the spectral structure at \sim TeV. The present spin-down luminosity $L_{\text{SD}} = 3.5 \times 10^{34}$ erg s $^{-1}$ and the characteristic age $t_{\text{age}} = 3.0 \times 10^5$ yr of the Geminga pulsar (Bertsch et al. 1992) imply an energy release of $L_{\text{SD}} t_{\text{age}} = 3.3 \times 10^{47}$ erg. The required energy release in the Geminga models (e.g. Fang et al. 2018) is $\sim 10^{49}$ erg, which may require a prompt energy release just at the pulsar’s birth.

If electron–positron pairs freely escape from the Geminga pulsar, it can account for the AMS-02 positron component (Yuan et al. 2017). However, such an efficient escape from PWNe is rejected for Vela X (Huang et al. 2018); the CR flux from Vela X would largely exceed the observed flux in this case. In addition, many pulsars were born after Geminga’s birth, and they should similarly contribute to the positron CR flux. If we adopt a similar model parameter set for other pulsars, the total positron flux may exceed the observed flux.

Gamma-ray observations show that the diffusion coefficient around the Geminga pulsar is largely suppressed (Abeysekara et al. 2017). In general, PWNe are surrounded by SNRs, and the CR energy density around nebulae is much higher than the average value in the interstellar space, which may be reasons for the suppressed diffusion coefficient. A large fraction of CRs released from Geminga may remain around the source yet. If we simply adopt the suppressed diffusion coefficient in Abeysekara et al. (2017) ($K_G = 3.2 \times 10^{26}$ cm 2 s $^{-1}$ at 100 GeV) and the gamma-ray halo size ($R_G \sim 50$ pc), the escape time of 100 GeV electrons from the Geminga halo is $R_G^2/(4K_G) \simeq 590$ kyr, which is longer than the age of Geminga. Although this estimate may be too pessimistic, we can assume a significant time-delay for the CR escape from PWNe.

Secondary CRs produced from proton CRs propagating in the interstellar medium are also the source of electron and positron CRs. Compared to the electron and positron flux, the contribution of such secondary CRs is negligible above 10 GeV (see e.g., Di Mauro et al. 2021). Even for the positron spectrum, the secondary CRs can be neglected above ~ 50 GeV, so that we omit the secondary electrons and positrons in this paper.

2.3. CR Flux at the Earth

Since the elapsed time to evolve from γ_0 to γ via radiative cooling is numerically calculated by

$$t_i(\gamma, \gamma_0) = \int_{\gamma}^{\gamma_0} d\gamma' \frac{m_e c^2}{b(\gamma')}, \quad (15)$$

we can produce a table of the initial Lorentz factor $\gamma_0(\gamma, t_i)$ as a function of the present Lorentz factor γ and the elapsed time t_i . We also produce a table for the diffusion radius defined as

$$r_{\text{dif}}(\gamma, t_i) = 2 \sqrt{\int_{\gamma}^{\gamma_0} d\gamma' \frac{m_e c^2 K(\gamma')}{b(\gamma')}}. \quad (16)$$

Using those tables numerically prepared in advance, we obtain the CR spectrum at the earth from a single source

(Atoyan et al. 1995) as

$$n_i(\gamma) = \frac{Q_i}{\pi^{3/2} r_{\text{dif}}^3} \frac{b(\gamma_0)}{b(\gamma)} \left(\frac{\gamma_0 m_e c^2}{\text{GeV}} \right)^{-\alpha} \times \exp\left(-\frac{\gamma_0}{\gamma_{\text{max}}}\right) \exp\left(-\frac{r_i^2}{r_{\text{dif}}^2}\right), \quad (17)$$

(see also e.g., Hooper et al. 2017).

As we explained above, the Klein–Nishina effect is numerically included in our method. Figure 1 shows the results of test calculations to comprehend the Klein–Nishina effect. If we neglect the Klein–Nishina effect, the cutoff energy is underestimated and the cutoff shape becomes sharper than the exact spectrum. Around a few TeV, the contributions from sources occurred ~ 100 kyr before are drastically different between the calculations with and without the Klein–Nishina effect.

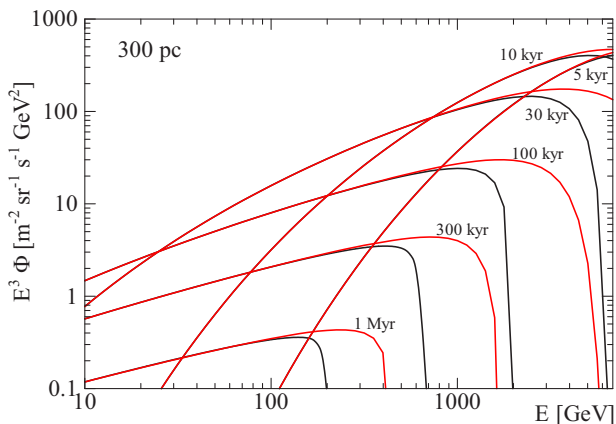


FIG. 1.— Electron spectra of a single source at $r = 300$ pc that released electrons 5 kyr, 10 kyr, 30 kyr, 100 kyr, 300 kyr, and 1 Myr ago. The red and black lines show the results with and without the Klein–Nishina effect, respectively. The parameters are $K_0 = 3.0 \times 10^{28} \text{ cm}^2 \text{ s}^{-1}$, $q = 1/3$, $E_{\text{tot}} = 10^{48} \text{ erg}$, $\alpha = 2.0$, and $\gamma_{\text{max}} m_e c^2 = 10 \text{ TeV}$.

Though Evoli et al. (2021) take into account the spiral structure of our galaxy for the source distribution, we simply assume constant and homogeneous rates of SNe in this paper. The scale height h is set as ± 300 pc, in which the SN rate is constant, and we neglect the contributions above or below this scale height. We integrate sources with the radial distance $R \leq 10$ kpc from the earth and $t_i \leq 10^8$ yr. The final electron and positron spectrum at the earth is calculated by summing up all the contributions of SNe as

$$\Phi(E) = \frac{c}{4\pi} \sum_i \frac{n_i(\gamma)}{m_e c^2}, \quad (18)$$

in unit of $\text{m}^{-2} \text{sr}^{-1} \text{s}^{-1} \text{GeV}^{-1}$.

3. MONTE CARLO RESULTS

First, we assume the Kolmogorov-type diffusion ($q = 1/3$), which is consistent with the B/C ratio observation with AMS-02 (Aguilar et al. 2016, 2018) and the preliminary CALET result (Akaike & Maestro 2021), though values $q = 0.41$ – 0.44 (Genolini et al. 2015; Kappl et al. 2015) or a broken power-law model (Evoli et al. 2019) are acceptable for the combined fit to the B/C ratio

and heavy nuclei. The normalization is assumed as $K_0 = 3.0 \times 10^{28} \text{ cm}^2 \text{ s}^{-1}$ (Strong et al. 2007).

As will be shown below, the Monte Carlo results show large variations of the spectral shape. For a certain parameter set, even when most of the results do not agree with the observed data, we may find a few percent of results consistent with the data. Considering this large dispersion in the Monte Carlo results and the simplified assumptions in our theoretical model, we do not quantitatively estimate how models agree with the data, as it would hardly yield useful information.

In §3.1, we test the simplest model; only one type of sources with a common injection index is considered. We obtain typical parameter values agreeing with the CALET spectrum. However, the spectral bump at 100–300 GeV and the sharp drop at ~ 1 TeV in the CALET spectrum require other types of sources with a different energy release and injection index. In §3.2, we add two components, one of which is consistent with the positron component measured with AMS-02, and another one for reproducing the sharp drop at ~ 1 TeV originating from an extraordinary source with a hard injection index. In §3.3, we test cases with a dispersion in the injection index for SNR sources. Our results roughly provide an allowed width of the injection index distribution. Based on this model, we also discuss the number of nearby sources contributing to the measured flux above 3 TeV. In §3.4, for reference, we show results for the Iroshnikov-Kraichnan type diffusion. The difference in the diffusion index does not change the main conclusions.

3.1. Constant Index

In this section, we show the results with a constant index of α as the simplest case. In Figure 2, we summarize the Monte Carlo results of 1000 trials with $\alpha = 2.58$. Though the injection parameters are fixed, the diversity of the spatial and age distributions leads to a variation in the spectral shape as shown by the blue dashed lines. A significant fraction of the trials and the average spectrum (the blue solid line) are consistent with the CALET electron and positron spectrum. When accidentally a few recent and nearby sources occur in a sample, the flux above ~ 1 TeV becomes significantly larger than the CALET flux. Such an example is the one with the highest flux among the three dashed lines in Figure 2. The variance of the spectrum is shown with the shaded region in the figure.

The assumed SN rate of $\mathcal{R} = 7.7 \times 10^{-2} \text{ kpc}^{-2} \text{ kyr}^{-1}$ corresponds to 1 SN per 510 yr within 3 kpc or equivalently 1 SN per 46 yr within 10 kpc for our choice of $E_{\text{tot}} = 9.0 \times 10^{47} \text{ erg}$. As the SN rate and E_{tot} are degenerate parameters, the essential parameter is the energy injection rate density of CR electrons, which is $\mathcal{R} E_{\text{tot}} = 6.9 \times 10^{46} \text{ erg kpc}^{-2} \text{ kyr}^{-1}$. A larger \mathcal{R} holding the constant value of $\mathcal{R} E_{\text{tot}}$ reduces the dispersion of the spectrum. However, a much larger value of \mathcal{R} is not realistic.

The spectral index 2.81 ± 0.03 of low-energy (< 300 GeV) protons measured with CALET (Adriani et al. 2019) and our injection index $\alpha = 2.58$ is roughly consistent with the similar injection indices for protons and electrons ($2.81 \pm 0.03 - q = 2.48 \pm 0.03$ for protons) in this Kolmogorov case.

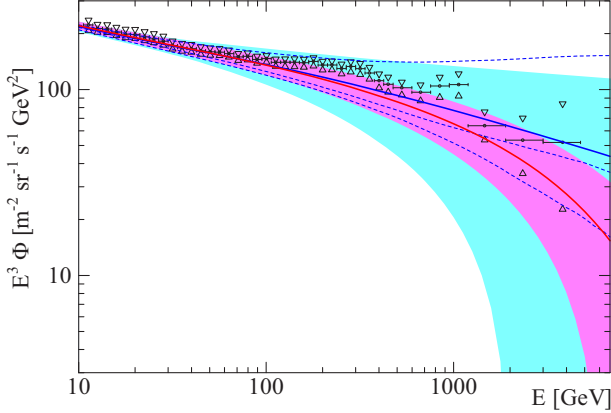


FIG. 2.— The Monte Carlo simulation results with a constant injection index $\alpha = 2.58$. The other parameters are SN rate of $7.7 \times 10^{-2} \text{ kpc}^{-2} \text{ kyr}^{-1}$, $K_0 = 3.0 \times 10^{28} \text{ cm}^2 \text{ s}^{-1}$, $q = 1/3$, and $E_{\text{tot}} = 9.0 \times 10^{47} \text{ erg}$. The maximum energy is assumed as infinity (blue) and $\gamma_{\text{max}} m_e c^2 = 10 \text{ TeV}$ (red). The observed data with CALET is taken from Adriani et al. (2018). The thick lines are the average spectrum of 1000 trials. The blue dashed lines are three examples of the trials for $\gamma_{\text{max}} = \infty$. The spectral variation (1σ) is shown with cyan and magenta regions, for blue and red average spectra, respectively.

Figure 2 shows two cases with and without the high-energy cutoff in the injection spectrum. The average spectra based on 1000 trials seem to prefer the model with the cutoff at 10 TeV. The model with the cutoff results in a narrower dispersion in the spectrum variance (compare the cyan and magenta regions in the figure). If a very nearby source was recently born, it dominates the CR flux above $\sim \text{TeV}$. Depending on the distance and age of such sources, the nearby sources produce a large dispersion in the spectrum. However, the cutoff in the spectra effectively reduces the relative contribution of the nearby sources, which reduces the dispersion as shown in the figure. As shown by the blue dashed lines, we can find several examples consistent with the observed data in our Monte Carlo trials without the cutoff. We cannot reject the model without cutoff at a level of at least 1σ .

3.2. Contribution of Electron–Positron Pair Sources

Though the single component model in §3.1 roughly reproduces the CALET spectrum, we do not find a result with a spectral modulation similar to the characteristic structures in the CALET spectrum, the 300 GeV bump and the $\sim 1 \text{ TeV}$ sharp drop, in our 1000 trials. Although those structures can be due to the statistical fluctuation, we try to reconcile them by adding other components in this section.

The bump-like structure around 300 GeV can be related to the positron component measured with AMS-02 (Aguilar et al. 2019). One of the most promising candidates for the positron sources are pulsars (e.g. Zhang & Cheng 2001; Grimani 2007; Hooper et al. 2009; Malyshev et al. 2009; Delahaye et al. 2010; Cholis et al. 2018; Di Mauro et al. 2021; Orusa et al. 2021). On the other hand, the sudden drop seen at $\sim 1 \text{ TeV}$ in the CALET spectrum may be attributed to a single source with a hard injection spectrum. The sharp structure may correspond to the spectral cutoff due to radiative cooling (Fujita et al. 2009; Kawanaka et al. 2010; Cholis & Hooper 2014; Kohri et al. 2016; Recchia et al. 2019). In this scenario,

the cutoff energy at $\sim 1 \text{ TeV}$ implies a prompt CR injection $\sim 400 \text{ kyr}$ ago.

As will be shown below, the single source required for the TeV sharp drop needs to release $\sim 10^{49} \text{ erg}$ as electrons and/or positrons. A very special source such as a hypernova remnant may directly accelerate electrons of $\sim 10^{49} \text{ erg}$, which is much larger than the E_{tot} we have adopted for the usual SNR CRs. Alternatively, we can consider an electron–positron pair source such as a SNR interacting with molecular clouds (Fujita et al. 2009; Kohri et al. 2016), or pulsars. The extrapolation from the positron spectrum with AMS-02 is not consistent with the TeV sharp drop. Models with a single electron–positron pair source predict that another component appears around 1 TeV in the positron spectrum. The extra component contributes to the AMS-02 positron flux at 800 GeV, unless the spectrum is extremely hard. We cannot uniquely divide the measured positron spectrum into the background due to pulsars and a nearby single component.

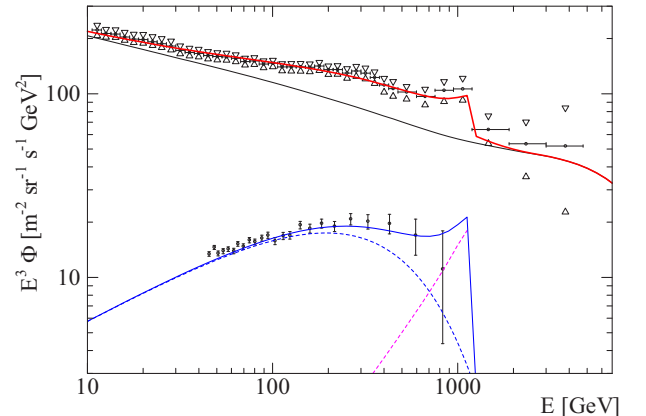


FIG. 3.— An example of model spectra with additional components consistent with the positron spectrum measured by AMS-02 (Aguilar et al. 2019). The red line is the sum of the electron–positron pair component (double the positron flux denoted with a blue solid line) and the SN electron component (black solid), which is a realization of the same Monte Carlo simulations as in Fig. 2 with $\gamma_{\text{max}} m_e c^2 = 10 \text{ TeV}$. The positron component (blue solid) is the sum of two components denoted with dashed lines. The blue dashed line is a positron component of $\Phi \propto E^{-2.45} \exp(-E/(350 \text{ GeV}))$, and the magenta dashed line is calculated from an electron–positron pair ejection which occurred 420 kyr ago at $r = 1 \text{ kpc}$ (source “S”), whose parameters are $E_{\text{tot}} = 1.5 \times 10^{49} \text{ erg}$, $\alpha = 1.5$, and $\gamma_{\text{max}} m_e c^2 = 100 \text{ TeV}$.

Figure 3 shows a synthesized spectrum of three components: one example of the electron spectrum chosen from the trials in the previous section (black solid), the pair component from pulsars (blue dashed for only positrons), and a hard pair component from a single nearby source (source “S”, magenta dashed for only positrons). The total positron spectrum of the two latter pair components is consistent with the AMS-02 positron spectrum, and the total electron plus positron spectrum agrees with the CALET spectrum, including the bump around 200–300 GeV and the sharp drop at $\sim 1 \text{ TeV}$. In the first 100 trials in our Monte Carlo simulations for electron CRs from SNe, we can find a few similar examples to that in Figure 3. Therefore, this example is not an extremely accidental case.

To reproduce the sharp drop at $\sim 1 \text{ TeV}$, in Fig-

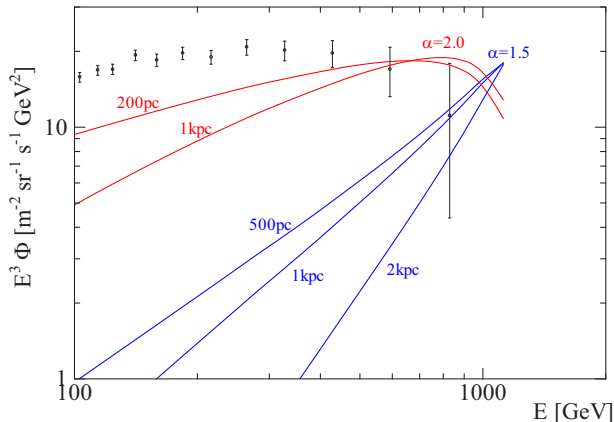


FIG. 4.— Model spectra of positrons from a single source 420 kyr ago (source “S”) with $K_0 = 3.0 \times 10^{28} \text{ cm}^2 \text{ s}^{-1}$, $q = 1/3$, and $\gamma_{\text{max}} m_e c^2 = 100 \text{ TeV}$. The blue lines are models of $\alpha = 1.5$ from various distances as denoted, for which the energy range is $E_{\text{tot}} = 1.1\text{--}5.1 \times 10^{49} \text{ erg}$. The red lines are models of $\alpha = 2.0$, for which the energy range is $E_{\text{tot}} = 1.7\text{--}3.0 \times 10^{49} \text{ erg}$.

ure 3, we inject pairs from the source “S” with an index of $\alpha = 1.5$ with the background pulsar component, for which we artificially assume a spectral shape of $\Phi \propto E^{-2.45} \exp(-E/(350\text{GeV}))$. If we change the source property of the source “S”, the background pulsar component should have another spectral shape. As shown in Figure 4, a softer injection spectrum of $\alpha = 2.0$ makes a spectral bump just below the cutoff energy at TeV, which is partially due to the Klein–Nishina effect. Softer injection spectra with $\alpha = 2.0$ for the single source are hard to reconcile with the sharp drop in the CALET spectrum, and the contribution to the AMS-02 positron spectrum seems too large as shown in Figure 4. The required total energy is $1.1\text{--}5.1 \times 10^{49} \text{ erg}$ for a distance of 0.5–2 kpc.

If the single source produced only electron CRs (e.g. electron acceleration at a hypernova remnant), the positron component can be attributed to only usual pulsars. In this case, we do not need to assume a different spectral shape from the AMS-02 spectrum as we did in Figure 3. The required value of E_{tot} for the source “S” is not largely changed even in this case. A slightly softer index can be possible, but it should be significantly harder than $\alpha = 2$ as shown in Figure 4.

Below we discuss the background pulsar component for the AMS-02 positron spectrum. A model with multiple-source contributions is natural for the positron component, too. We reproduce the model spectrum for this component assumed in Figure 3 with the same Monte Carlo method. While several studies claimed that the radio pulsar birth rate is close to the SN rate in our galaxy (Faucher-Giguère & Kaspi 2006), not all SNe leave an active pulsar or a PWN (e.g. 1987A and Cassiopeia A, see Alp et al. 2021; Chakrabarty et al. 2001). Lorimer et al. (1993) estimated the local pulsar birth rate density as $0.6\text{--}1.2 \times 10^{-2} \text{ kpc}^{-2} \text{ kyr}^{-1}$, which is ~ 10 times lower than the SN rate density we have assumed. The fraction of high magnetic field or active pulsars may be significantly lower (Vranesevic et al. 2004; Lorimer et al. 2006). Here we assume the birth rate of active pulsars as positron sources as $1.0 \times 10^{-2} \text{ kpc}^{-2} \text{ kyr}^{-1}$. As we have discussed in §2.2, we consider that positrons from

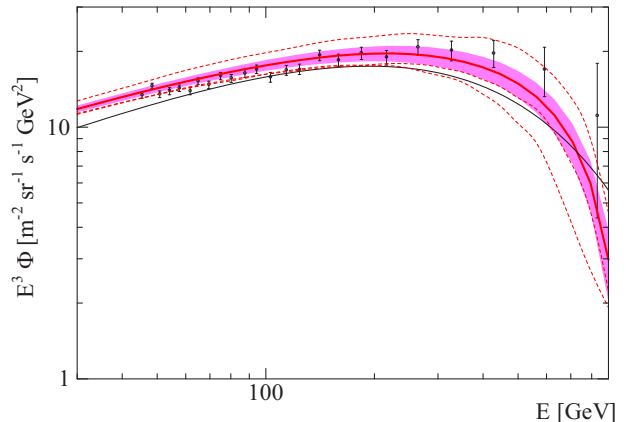


FIG. 5.— Positron spectra obtained from multiple pair release events with a rate of $1.0 \times 10^{-2} \text{ kpc}^{-2} \text{ kyr}^{-1}$, $K_0 = 3.0 \times 10^{28} \text{ cm}^2 \text{ s}^{-1}$, $q = 1/3$, $E_{\text{tot}} = 6.5 \times 10^{47} \text{ erg}$, $\alpha = 1.9$, and $\gamma_{\text{max}} m_e c^2 = 10 \text{ TeV}$. We have assumed that no event within the last 500 kyr contributes to the positron flux. The red thick line is the average spectrum of 1000 trials. The red dashed lines are three examples of the trials. The black line is the model spectrum assumed in Figure 3.

the Geminga pulsar at $r = 0.25 \text{ kpc}$, whose age is 342 kyr, do not largely contribute to the AMS-02 positron spectrum yet. Thus, we assume that no event within the last 500 kyr contributes to the positron spectrum, which is preferable for the spectral peak at 200–300 GeV.

The results are shown in Figure 5. The average spectral shape of the CRs from pulsars (red solid line) is roughly consistent with the observed data from AMS-02 and the model spectrum other than the distribution of source “S” assumed in Figure 3 (the blue dashed line in Figure 3 and the black line in Figure 5 are the same). Also in this case, the spectral shape fluctuates depending on trials. Even with a constant parameter set, we can find several trials that produce a spectrum close to, or lower, than the model assumed in Figure 3. The required parameters are $\alpha = 1.9$ and $E_{\text{tot}} = 6.5 \times 10^{47} \text{ erg}$ ($\mathcal{R}E_{\text{tot}} = 6.5 \times 10^{45} \text{ erg kpc}^{-2} \text{ kyr}^{-1}$). If we take into account the secondary positrons we have neglected in our calculations, the injection index can be harder than 1.9. The energy per pulsar is close to the Geminga’s value of $L_{\text{SD}} t_{\text{age}}$. While we have assumed a constant E_{tot} , Evoli et al. (2021) considered a Gaussian distribution in the initial spin period. The average energy release in Evoli et al. (2021) is $1.5 \times 10^{47} \text{ erg}$ with an average initial spin period of 100 ms. This lower value than ours is due to the higher birth rate they adopted. Thus, although the value of E_{tot} depends on the effective pulsar birth rate, it may not largely exceed 10^{48} erg .

The injection spectral index α for the pulsar component is required to be significantly harder than the index for SNRs. This may be attributed to the intrinsic acceleration properties of pulsar CRs or the escape process from PWNe.

The source “S” for the TeV sharp drop requires a harder injection spectrum ($\alpha \geq 1.5$) and a larger energy release ($E_{\text{tot}} > 10^{49} \text{ erg}$) than those for the background pulsars. Therefore, if this source really exists, it belongs to another peculiar type of population different from usual pulsars. As discussed in Kohri et al. (2016), a peculiar type of event, such as a supernova with an efficient secondary pair production via interaction with

molecular cloud, is required.

If the events like the source “S” occur with a rate of 1/100 of the SN rate, the contribution from such sources to the positron spectrum at 300 GeV is higher than the observed one. To avoid the flux excess due to the stacking contribution of such hard sources, the rate should be lower than 1/300 of the SN rate. This implies that the rate of source “S”-type events is lower than once per 344 kyr within 2 kpc from us. Our assumption of the event 420 kyr ago does not contradict this rate. The upper limit of the rate is also roughly consistent with the occurrence rate of broad-line Ibc SNe or hypernovae (Guetta & Della Valle 2007).

3.3. Dispersion in the injection index

While we have assumed a constant value for the injection index of electron CRs from SNRs, the real indices of the escaped electron CRs can have a dispersion. From radio spectral indices in SNRs, Clark & Caswell (1976) found a dispersion in the non-thermal electron index of $\sigma_\alpha \sim 0.3$. The spectral index of electron CRs can be affected by the escape process (Ohira et al. 2010, 2012) and/or radiative cooling (Diesing & Caprioli 2019; Morlino & Celli 2021). The dispersion of the injection index can produce a modulation in the spectral shape. The required property for the source “S” can be altered by such a modulation.

Here we assume a Gaussian probability distribution for the index α ,

$$P(\alpha) \propto \exp[-(\alpha - \bar{\alpha})^2 / (2\sigma_\alpha^2)], \quad (19)$$

where constants $\bar{\alpha}$ and σ_α are the average index and dispersion, respectively. The number of trials to plot the average spectra is 100 in Figure 6. This trial number is significant for our purpose.

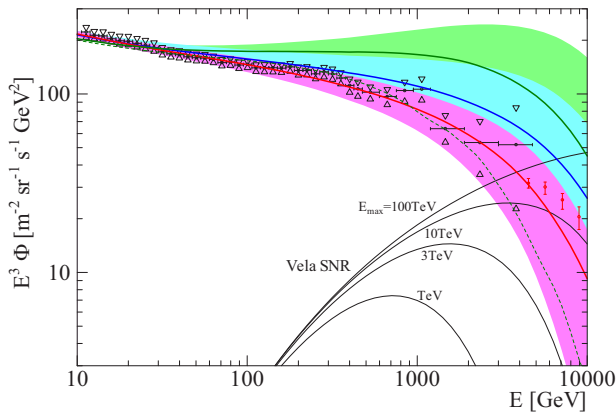


FIG. 6.— The Monte Carlo simulation results with Gaussian distribution for α ($\bar{\alpha} = 2.58$). Other parameters are the same as those in Figure 2: SN rate of $7.7 \times 10^{-2} \text{ kpc}^{-2} \text{ kyr}^{-1}$, $K_0 = 3.0 \times 10^{28} \text{ cm}^2 \text{ s}^{-1}$, $q = 1/3$, $E_{\text{tot}} = 9.0 \times 10^{47} \text{ erg}$, and $\gamma_{\text{max}} m_e c^2 = 10 \text{ TeV}$. The thick lines are the average spectra of 100 trials with $\sigma_\alpha = 0.15$ (red), 0.2 (blue), and 0.3 (green). The spectral variation (1σ) is shown with light green, cyan and magenta regions, for green, blue and red average spectra, respectively. The green dashed line is an example of the trials for $\sigma_\alpha = 0.3$. The red data points are indirect measurements of electrons and positrons by H.E.S.S. Collaboration (2017). The Vela SNR spectra (black) are calculated with the distance of 287 pc, the age 10 kyr, $E_{\text{tot}} = 9.0 \times 10^{47} \text{ erg}$, $\alpha = 2.52$, and various $E_{\text{max}} = \gamma_{\text{max}} m_e c^2$.

As shown in Figure 6, even with the dispersion in α , the spectral index around 10 GeV is almost the same as in the case without dispersion. However, a broader distribution (larger σ_α) tends to produce a harder spectrum above 100 GeV, because contributions from harder components dominate in the high energy region. Sources with a softer index than $\bar{\alpha}$ do not contribute to the spectrum above $\sim \text{TeV}$ very much. The average spectrum for $\sigma_\alpha = 0.3$ seems too hard. However, the dispersion in spectral shapes is large. In the first 100 trials for $\sigma_\alpha = 0.3$, we can find an example consistent with the CALET spectrum, as shown by the green dashed line.

The data from the H.E.S.S. Collaboration (2017) plotted in Figure 6 is unique data in this energy range. However, the H.E.S.S. results are preliminary, and show very small errors in spite the measurement being indirect. They are qualitatively different data sets, so we treat the H.E.S.S. data points as referential data in this paper.

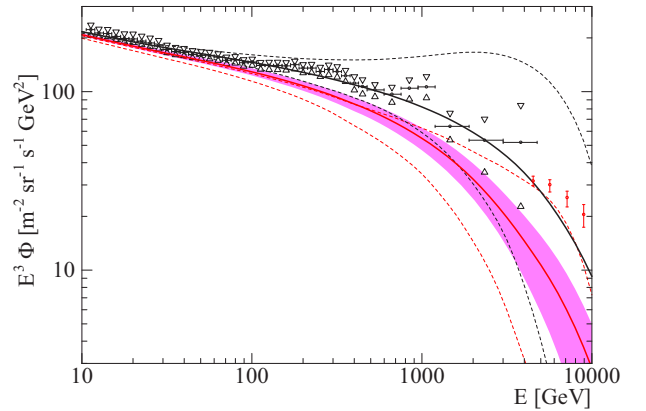


FIG. 7.— The spectra with and without the contributions from nearby sources. The thick black line is the same average spectrum for $\sigma_\alpha = 0.15$ in Figure 6. The black dashed lines are two examples of the trials. The red lines show the results excluding events within 500 pc and 100 kyr, for which the average of 100 trials (thick) and two examples of the trials (dashed) are shown. The spectral variation (1σ) corresponding to the red solid line is shown with the magenta region, respectively.

Figure 6 also shows model spectra for the Vela SNR, which has been discussed as a possibly dominant source in the TeV energy range in previous studies (e.g., Kobayashi et al. 2004; Kawanaka et al. 2011; Manconi et al. 2019; Fornieri et al. 2020). As we assumed in Figure 6, if Vela’s electron injection is close to the average properties of other SNRs, we may have already detected electron CRs from the Vela SNR, depending on the cutoff energy. However, the large dispersion in the spectrum makes it difficult to definitely distinguish individual nearby sources. Similarly to the leptonic CRs from pulsars, a significant delay of CR escape may be possible even for the Vela SNR. The delay can further diminish the flux of Vela.

Figure 7 shows the contribution of relatively distant sources above $\sim \text{TeV}$. The red lines show cases where nearby sources with ($r_i < 500 \text{ pc}$) \cap ($t_i < 100 \text{ kyr}$) are artificially excluded. The differences between red and black lines show the contribution of the recent nearby sources. Although the red lines tend to be lower than the fluxes shown with black lines, Figure 7 shows a significant contribution of distant ($r_i > 500 \text{ pc}$) sources to

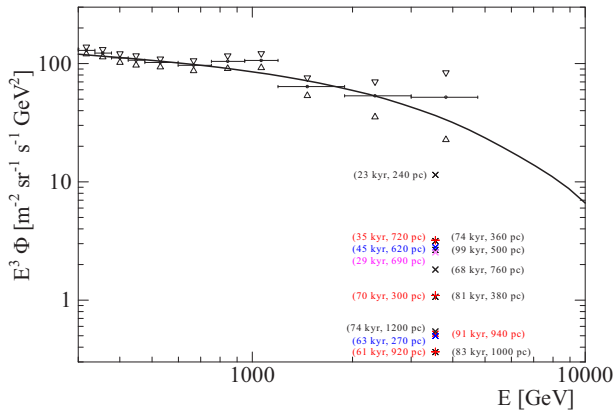


FIG. 8.— An example of trials for $\sigma_\alpha = 0.15$. The parameters are the same as those in Figure 6. Contributions to the 3.5 TeV flux from individual sources are denoted by crosses. The top 14 flux contributions are plotted with the age and distance of the sources. To distinguish each contribution, we change the color and symbol especially for overlapping points.

the flux above \sim TeV. Such sources may be hard to identify observationally as a possible source.

Let us consider sources whose contribution to the last energy bin at 3.5 TeV is larger than $3.5 \text{ m}^{-2} \text{ sr}^{-1} \text{ s}^{-1} \text{ GeV}^2$, which is 15% of the lower value of the CALET fluxes with errors. Hereafter, we call such sources “primary contributors at 3.5 TeV”. For the case of $\sigma_\alpha = 0.15$, the average source number of the primary contributors is 2.3. The average age and the distance of the primary contributors at 3.5 TeV are 39 ± 22 kyr and 400 ± 150 pc. Therefore, a few distant ($\gtrsim 500$ pc) sources largely contribute to the flux at 3.5 TeV. However, only the contribution of such primary sources does not account for most of the flux at 3.5 TeV in general.

Figure 8 shows one typical example of the flux contributions from individual sources. In this case, the number of primary contributors at 3.5 TeV is only one coming from a source at 240 pc. This source contributes $\sim 1/3$ of the CALET flux at 3.5 TeV. The residual $\sim 2/3$ of the CALET flux are attributed to the sum of ~ 10 weak sources.

3.4. Iroshnikov-Kraichnan Diffusion

We have assumed Kolmogorov type diffusion. In this section, to check the dependence on the spatial diffusion property, we apply Iroshnikov–Kraichnan (IK) type diffusion, $q = 1/2$ with the diffusion coefficient of $K_0 = 2.08 \times 10^{28} \text{ cm}^2 \text{ s}^{-1}$ (Yuan et al. 2017; Fang et al. 2018b). The analytic estimate suggests a harder injection spectral index $\Delta\alpha = (0.5 - 0.33)/2 \simeq 0.08$. As expected, an index of $\bar{\alpha} = 2.50$ agrees with the CALET spectrum as shown in Figure 9. However, the implied proton injection index ($2.81 \pm 0.03 - q = 2.31 \pm 0.03$) is significantly harder than $\bar{\alpha} = 2.50$. For the IK diffusion, the radiative cooling effect on the escape process of electrons (Diesing & Caprioli 2019; Morlino & Celli 2021) may have to be taken into account.

The obtained spectra are similar to the cases for $q = 1/3$ (Figure 6). To fit the CALET spectrum, we adopt a slightly lower birth rate ($7.0 \times 10^{-2} \text{ kpc}^{-2} \text{ kyr}^{-1}$, $\mathcal{R}E_{\text{tot}} = 6.3 \times 10^{46} \text{ erg kpc}^{-2} \text{ kyr}^{-1}$) than in the case for $q = 1/3$. A larger σ_α tends to produce a harder spectrum, but we can find a few cases consistent with the

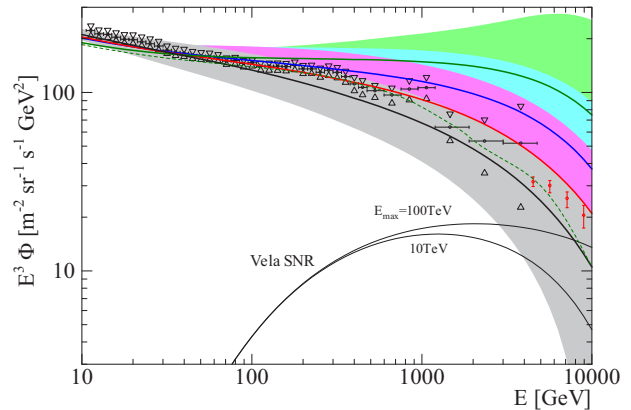


FIG. 9.— Same as Figure 6 but for $q = 1/2$. The parameters are SN rate of $7.0 \times 10^{-2} \text{ kpc}^{-2} \text{ kyr}^{-1}$, $K_0 = 2.08 \times 10^{28} \text{ cm}^2 \text{ s}^{-1}$, $\bar{\alpha} = 2.50$, $E_{\text{tot}} = 9.0 \times 10^{47} \text{ erg}$, and $\gamma_{\text{max}} m_e c^2 = 10 \text{ TeV}$. The thick lines are the average spectra of 100 trials with $\sigma_\alpha = 0$ (black), 0.15 (red), 0.2 (blue), and 0.3 (green). The spectral variation (1σ) is shown with grey, light green, cyan and magenta regions, for green, blue, red, and black average spectra, respectively. The green dashed line is an example of the trials for $\sigma_\alpha = 0.3$. The Vela SNR spectra (black) are calculated with the distance of 287 pc, the age 10 kyr, $E_{\text{tot}} = 9.0 \times 10^{47} \text{ erg}$, $\alpha = 2.52$, and various $E_{\text{max}} = \gamma_{\text{max}} m_e c^2$.

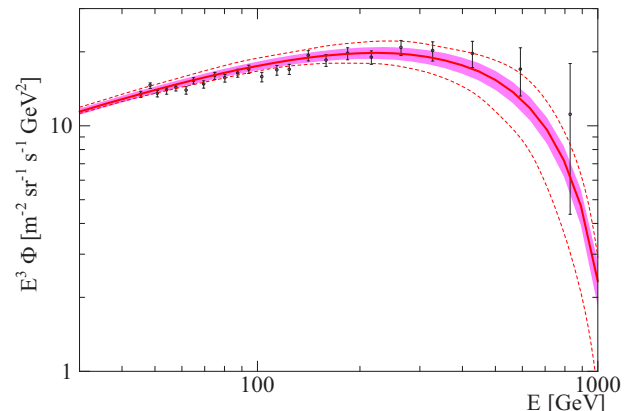


FIG. 10.— Positron spectra for $q = 1/2$ obtained from multiple pair release events with a rate of $1.0 \times 10^{-2} \text{ kpc}^{-2} \text{ kyr}^{-1}$, $K_0 = 2.08 \times 10^{28} \text{ cm}^2 \text{ s}^{-1}$, $E_{\text{tot}} = 8.0 \times 10^{47} \text{ erg}$, $\alpha = 1.8$, and $\gamma_{\text{max}} m_e c^2 = 10 \text{ TeV}$. We have assumed that no event within the last 400 kyr contributes to the positron flux. The red thick line is the average spectrum of 1000 trials. The spectral variation (1σ) is shown with the magenta region. The red dashed lines are two examples of the trials.

CALET spectrum even for $\sigma_\alpha = 0.3$ from 100 trials (see the green dashed line). The contribution from Vela SNR for $q = 1/2$ is lower than the model flux with $q = 1/3$.

The positron spectrum is also reproduced by this diffusion model with $\alpha = 1.8$ as shown in Figure 10. A slightly larger energy release ($8.0 \times 10^{47} \text{ erg per pulsar}$, $\mathcal{R}E_{\text{tot}} = 8.0 \times 10^{45} \text{ erg kpc}^{-2} \text{ kyr}^{-1}$) is required compared to the Kolmogorov case.

4. SUMMARY

Focusing on the electron and positron spectrum measured with CALET, we have carried out Monte Carlo simulations of random births of SNe and PWNe, and calculated the propagation of CRs to the earth including the Klein–Nishina effect on the CR cooling. This method can take into account the stochastic property of births of

nearby sources, which dominantly contribute to the CR flux above TeV. Our results are summarized as follows:

- A simple power-law energy dependence of the diffusion coefficient can account for the CALET spectrum. At least from the electron and positron spectrum alone, we do not find strong evidence for the broken power-law dependence.
- A cutoff at 10 TeV in the injection spectrum is favorable, but the CALET spectrum does not necessarily require a cutoff.
- In the case of Kolmogorov type diffusion, the local SN rate is $7.7 \times 10^{-2} \text{ kpc}^{-2} \text{ kyr}^{-1}$ for an energy release per SN of $E_{\text{tot}} = 9.0 \times 10^{47} \text{ erg}$, and a diffusion coefficient of $K_0 = 3.0 \times 10^{28} \text{ cm}^2 \text{ s}^{-1}$. In the case of Iroshnikov–Kraichnan type diffusion, the local SN rate is $7.0 \times 10^{-2} \text{ kpc}^{-2} \text{ kyr}^{-1}$ for $E_{\text{tot}} = 9.0 \times 10^{47} \text{ erg}$ and $K_0 = 2.08 \times 10^{28} \text{ cm}^2 \text{ s}^{-1}$.
- In the case of Kolmogorov type diffusion, the average injection index is 2.58 for SN electrons, while the plausible index for SN protons is 2.48. On the other hand, in the case of Iroshnikov–Kraichnan type diffusion, the indices are 2.50, and 2.31 for electrons and protons, respectively. The slightly softer injection spectrum for electrons may be attributed to the cooling effect at the escape from sources.
- Depending on Monte Carlo trials, the spectrum above $\sim \text{TeV}$ shows large variance. A larger dispersion of the injection index tends to produce a harder spectrum than the CALET spectrum especially above $\sim \text{TeV}$. A dispersion of the index larger than $\sigma_\alpha = 0.3$ is not favorable, but we can find several spectra consistent with the CALET spectrum from 100 Monte Carlo trials even for $\sigma_\alpha = 0.3$.
- The CALET flux for 2–4 TeV does not contradict CRs from SNRs. We do not need extraordinary sources to reproduce the flux in this energy range. One to three nearby SNRs, possibly including the Vela SNR, can contribute to a few tens of percent

of the observed flux. However, it is not likely that a single source accounts for almost all the flux in this energy range. Many SNRs at a distance $\gtrsim 500 \text{ pc}$ within 100 kyr account for the remaining several tens of percent of the observed flux.

- The characteristic bump structure around 200–300 GeV in the CALET spectrum is consistent with the additional component of electron–positron CRs measured with AMS-02. The energy injection rate of the pair CRs is $\gtrsim 5.0 \times 10^{45} \text{ erg kpc}^{-2} \text{ kyr}^{-1}$. The injection index is 1.8–1.9. If the sources for positrons are PWNe, the delayed CR escape from PWNe with a timescale of a few hundreds kyr is favorable. The released energy per pulsar may not exceed 10^{48} erg .
- The sharp drop at $\sim 1 \text{ TeV}$ in the CALET spectrum can be reproduced by an extraordinary event with a CR release $\sim 400 \text{ kyr}$ ago. The required energy and the injection index are $> 10^{49} \text{ erg}$ and 1.5, respectively. Those parameters are apparently different from those required for SNRs and PWNe. The rate of such extraordinary events should be lower than 1/300 of the rate of usual SNe.

The event rate of the sources required for the TeV sharp drop is roughly consistent with the rate of broad-line Ibc SNe or hypernovae. Alternatively, an accidentally efficient production of secondary electron and positron CRs may have occurred in a SN event via interaction with molecular clouds (Kohri et al. 2016). The TeV sharp drop is still seen in the updated CALET spectrum (Torii & Akaike 2021). We have tested our results with this preliminary data, and confirmed that the results are unchanged. A further improvement of the statistics in the CALET data will verify the significance of the sharp drop.

We gratefully acknowledge the support from the CALET collaboration team. This work is supported by the joint research program of the Institute for Cosmic Ray Research (ICRR), the University of Tokyo.

REFERENCES

- Abeysekara, A. U., Albert, A., Alfaro, R., et al. 2017, *Science*, 358, 911
- Abdollahi, S., Ackermann, M., Ajello, M., et al. 2017, *Phys. Rev. D*, 95, 082007
- Ambrosi, G., An, Q., Asfandiyarov, R., et al. 2017, *Nature*, 552, 63
- Adriani, O., Barbarino, G. C., Bazilevskaya, G. A., et al. 2011, *Phys. Rev. Lett.*, 106, 201101
- Adriani, O., Akaike, Y., Asano, K., et al. 2017, *Phys. Rev. Lett.*, 119, 181101
- Adriani, O., Akaike, Y., Asano, K., et al. 2018, *Phys. Rev. Lett.*, 120, 261102
- Adriani, O., Akaike, Y., Asano, K., et al. 2019, *Phys. Rev. Lett.*, 122, 181102
- Akaike, Y., & Maestro, P. 2021, *PoS(ICRC2021)112*
- Accardo, L., Aguilar, M., Aisa, D., et al. 2014, *Phys. Rev. Lett.*, 113, 121101
- Aguilar, M., Aisa, D., Alpat, B., et al. 2014, *Phys. Rev. Lett.*, 113, 221102
- Aguilar, M., Ali Cavasonza, L., Ambrosi, G., et al. 2016, *Phys. Rev. Lett.*, 117, 231102
- Aguilar, M., Ali Cavasonza, L., Ambrosi, G., et al. 2018, *Phys. Rev. Lett.*, 120, 021101
- Aguilar, M., Ali Cavasonza, L., Alpat, B., et al. 2019, *Phys. Rev. Lett.*, 122, 101101
- Alp, D., Larsson, J., & Fransson, C. 2021, *ApJ*, 916, 76
- Atoyan, A. M., Aharonian, F. A., & Völk, H. J. 1995, *Phys. Rev. D*, 52, 3265
- Bertsch, D. L., Brazier, K. T. S., Fichtel, C. E., et al. 1992, *Nature*, 357, 306
- Blumenthal, G. R., & Gould, R. J. 1970, *Rev. Mod. Phys.*, 42, 237
- Clark, D. H., & Caswell, J. L. 1976, *MNRAS*, 174, 267
- Chang, J., Adams, J. H., Ahn, H. S., et al. 2008, *Nature*, 456, 362
- Cholis, I., & Hooper, D., 2014, *Phys. Rev. D*, 89, 043013
- Cholis, I., Karwal, T., & Kamionkowski, M., 2018, *Phys. Rev. D*, 98, 063008
- Delahaye, T., Lavalle, J., Lineros, R., Donato, F., & Fornengo, N. 2010, *A&A*, 524, A51
- Di Mauro, M., Donato, F., & Manconi, S. 2021, *Phys. Rev. D*, 104, 083012
- Diesing, R., & Caprioli, D. 2019, *Phys. Rev. Lett.*, 123, 071101

- Ding, Y.-C., Nan, L., Wei, C.-C., Wu, Y.-L., & Zhou, Y.-F., 2021, Phys. Rev. D, 103, 115010
- DuVernois, M. A., Barwick, S. W., Beatty, J. J., et al. 2001, ApJ, 559, 296
- Evoli, C., Aloisio, R., & Blasi, P. 2019, Phys. Rev. D, 99, 103023
- Evoli, C., Blasi, P., Amato, E., & Aloisio, R. 2020, Phys. Rev. Lett., 125, 051101
- Evoli, C., Amato, E., Blasi, P., & Aloisio, R. 2021, Phys. Rev. D, 103, 083010
- Fang, K., Bi, X.-J., & Yin, P.-F. 2018, ApJ, 854, 57
- Fang, K., Bi, X.-J., Yin, P.-F., & Yuan, Q. 2018, ApJ, 863, 30
- Fang, K., Bi, X.-J., Lin, S.-J., & Yuan, Q. 2021, Chin. Phys. Lett., 38, 039801
- Faucher-Giguère, C.-A., & Kaspi, V. M. 2006, ApJ, 643, 332
- Chakrabarty, D., Pivovarov, M. J., Hernquist, L. E., Heyl, J. S., & Narayan, R. 2001, ApJ, 548, 800
- Fornieri, O., Gaggero, D., & Grasso, D. 2020, JCAP, 02(2020), 009
- Fujita, Y., Kohri, K., Yamazaki, R., & Ioka, K. 2009, Phys. Rev. D, 80, 063003
- Genolini, Y., Putze, A., Salati, P., & Serpico, P. D. 2015, A&A, 580, A9
- Guetta, D., & Della Valle, M. 2007, ApJ, 657, L73
- Grimani, C. 2007, A&A, 474, 339
- H.E.S.S. Collaboration 2017, 35th ICRC, Busan, South Korea, CRI215
- Hooper, D., Blasi, P., & Serpico, P. D. 2009, JCAP, 01(2009), 025
- Hooper, D., Cholis, I., Linden, T., & Fang, K. 2017, Phys. Rev. D, 96, 103013
- Huang, Z.-Q., Fang, K., Liu, R.-Y., & Wang, X.-Y. 2018, ApJ, 866, 143
- Kappl, R., Reinert, A., & Winkler, M. W. 2015, JCAP, 10(2015), 034
- Kashiyama, K., Ioka, K., & Kawanaka, N. 2011, Phys. Rev. D, 83, 023002
- Kawanaka, N., Ioka, K., & Nojiri, M. M. 2010, ApJ, 710, 958
- Kawanaka, N., Ioka, K., Ohira, Y., & Kashiyama, K. 2011, ApJ, 729, 93
- Keane, E. F., & Kramer, M. 2008, MNRAS, 391, 2009
- Kisaka, S., & Kawanaka, N. 2011, MNRAS, 421, 3543
- Kobayashi, T., Komori, Y., Yoshida, K., & Nishimura, J. 2004, ApJ, 601, 340
- Kohri, K., Ioka, K., Fujita, Y., & Yamazaki, R. 2016, PTEP, 2016, 021E01
- Lipari, P. 2019, Phys. Rev. D, 99, 043005
- Lorimer, D. R., Bailes, M., Dewey, R. J., & Harrison, P. A. 1993, MNRAS, 263, 403
- Lorimer, D. R., Faulkner, A. J., Lyne, A. G., et al. 2006, MNRAS, 372, 777
- Malyshev, D. Cholis, I., & Gelfand, J. 2009, Phys. Rev. D, 80, 063005
- Manconi, S., Di Mauro, M., & Donato, F. 2019, JCAP, 04(2019), 024
- Mertsch, P. 2018, JCAP, 11(2018), 045
- Morlino, G., & Celli, S. 2021, arXiv:2106.06488
- Ohira, Y., Murase, K., & Yamazaki, R. 2010, A&A, 513, A17
- Ohira, Y., Yamazaki, R., Kawanaka, N., & Ioka, K. 2012, MNRAS, 427, 91
- Orusa, L., Manconi, S., Donato, F., & Di Mauro, M. 2021, arXiv:2107.06300
- Recchia, S., Gabici, S., Aharonian, F. A., & Vink, J. 2019, Phys. Rev. D, 99, 103022
- Shi, Z.-D., & Liu, S. 2019, MNRAS, 485, 3869
- Strong, A. W., Moskalenko, I. V., & Ptuskin, V. S., 2007, Ann. Rev. Nuc. Part. Sci., 57, 285
- Torii, S., & Akaike, Y. 2021, PoS(ICRC2021)105
- Torii, S., Tamura, T., Tateyama, N., et al. 2001, ApJ, 559, 973
- Vranesevic, N., Manchester, R. N., Lorimer, D. R., et al. 2004, ApJ, 617, L139
- Yoshida, K., Torii, S., Yamagami, T., et al. 2008, Adv. Space Res., 42, 1670
- Yuan, Q., Lin, S.-J., Fang, K., & Bi, X.-J. 2017, Phys. Rev. D, 95, 083007
- Yüksel, H., Kistler, M. D., & Stanev, T. 2009, Phys. Rev. Lett., 103, 051101
- Zhang, L., & Cheng, K. S. 2001, A&A, 368, 1063